Chemical Science

ROYAL SOCIETY OF CHEMISTRY

EDGE ARTICLE

View Article Online
View Journal | View Issue

Check for updates

Cite this: *Chem. Sci.*, 2020, **11**, 4374

All publication charges for this article have been paid for by the Royal Society of Chemistry

Received 11th January 2020
Accepted 9th April 2020

DOI: 10.1039/d0sc00206b

rsc.li/chemical-science

Self-assembly of reversed bilayer vesicles through pnictogen bonding: water-stable supramolecular nanocontainers for organic solvents†

Shiva Moaven, Brandon T. Watson, Shelby B. Thompson, Veronica J. Lyons, Daniel K. Unruh, Dominick J. Casadonte, Dimitri Pappas and Anthony F. Cozzolino *

A new air and moisture stable antimony thiolate compound has been prepared that spontaneously forms stable hollow vesicles. Structural data reveals that pnictogen bonding drives the self-assembly of these molecules into a reversed bilayer. The ability to make these hollow, spherical, and chemically and temporally stable vesicles that can be broken and reformed by sonication allows these systems to be used for encapsulation and compartmentalisation in organic media. This was demonstrated through the encapsulation and characterization of several small organic reporter molecules.

Open Access Article. Published on 09 April 2020. Downloaded on 1/22/2026 8:31:17 PM.
This article is licensed under a Creative Commons Attribution-NonCommercial 3.0 Unported Licence.

Introduction

Storage and delivery of different compounds for medicinal applications, chemical reactions and analysis, cosmetics, and coatings is of great importance.[1–4] Biological systems have developed a very useful tool to achieve this. Biological cell membranes can compartmentalize into different sizes (nano to micrometre) of vesicles to protect and transport the different components of life within a physiological medium.[5] Non-aqueous environments play a dominant role in synthetic chemistry and different approaches are being investigated for the preparation of vesicles amenable to these environments. The real and perceived applications of these include synthetic cells,[5–7] nanocontainers[1,3,8,9] and nanoreactors.[1,10] These vesicles can be prepared using either covalent (polymers, metal-coordinated amphiphiles)[11–16] or non-covalent (dendrimers, phospholipids, polymers)[7,17–21] strategies. Polymersomes and metal-coordinated amphiphiles have proven to be useful in organic solutions for carrying and delivering their cargoes. Non-covalent interactions can be used to self-assemble reversed vesicles with more dynamic behaviour. Hydrogen bonding (HB)[22,23] and pnictogen bonding (PnB)[24] have also been successfully applied to this problem.

In this paper, an antimony thiolate cage, Sb-$\mathbf{1}_{Et}$ is prepared and its ability to form stable vesicles mediated by pnictogen bonding is studied. We contrast this to our previously reported bicyclic antimony alkoxide compounds (Sb-$\mathbf{2}_{Pr}$ and Sb-$\mathbf{2}_{NHCONon}$) that self-assemble into reversed bilayers facilitated by pnictogen bonding (Fig. 1).[24,25] Sonication of crystalline Sb-$\mathbf{2}_{NHCONon}$ under strictly anhydrous conditions resulted in the formation of reversed bilayer vesicles with an average diameter of 70 nm.[24] These compounds represent a well-behaved model system that allows for careful study, but they are susceptible to hydrolysis at the Sb–O bonds. This imposes limits on the future application of these unique supramolecular structures. Stibnite (Sb_2S_3) is one of the most stable and abundant sources of antimony.[26] Unlike the oxide analogue (Sb_2O_3), stibnite favours formation of ribbons. The presence of PnBs between ribbon layers has been recognized previously suggesting that a thiol analogue of the previously studied antimony alkoxides might

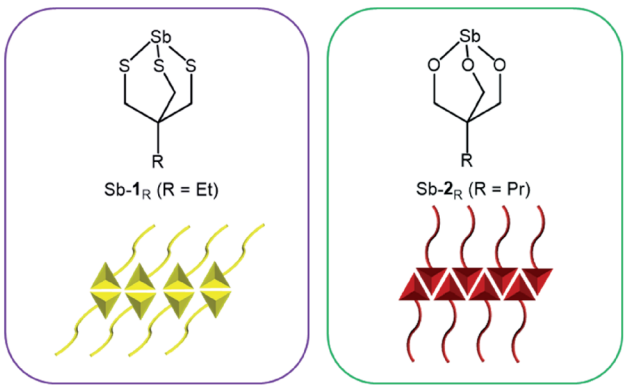

Fig. 1 Antimony thiolate cage (left) and previously reported antimony alkoxide cage[25] (right) and depiction of pnictogen-bonded bilayer motifs that they each form (bottom).

Department of Chemistry and Biochemistry, Texas Tech University, Box 41061, Lubbock, Texas 79409-1061, USA. E-mail: Anthony.f.cozzolino@ttu.edu

† Electronic supplementary information (ESI) available: Synthesis and preparation of materials and vesicles, ^{1}H NMR, ^{13}C NMR, ATR-FTIR, DLS, TEM, SEM, fluorescence microscopy. Cartesian coordinates of optimized molecules. CCDC 1976847. For ESI and crystallographic data in CIF or other electronic format see DOI: 10.1039/d0sc00206b

This journal is © The Royal Society of Chemistry 2020

Open Access Article. Published on 09 April 2020. Downloaded on 1/22/2026 8:31:17 PM.
This article is licensed under a Creative Commons Attribution-NonCommercial 3.0 Unported Licence.

still self-assemble.[27–29] Synthesis of antimony thiolates was envisioned as an approach to engender moisture stability[30–32] in these compounds while retaining the ability to self-assemble into reversed bilayers.

Synthesis and characterization of a trivalent antimony thiolate

Treatment of $H_3\mathbf{1}_{Et}$ with antimony tris-*tert*-butoxide (see S1.2 in ESI†) in anhydrous THF or hexanes results in the formation of Sb-$\mathbf{1}_{Et}$ (Scheme 1). Compound Sb-$\mathbf{1}_{Et}$ is confirmed by the loss of the band at 2552 cm^{-1} (Fig. S16†) associated with the S–H bond stretching vibration and disappearance of the chemical shift signal at 2.21 ppm (Fig. S7†) in the FTIR and ^{1}H NMR spectra, respectively. This is accompanied by the formation of *tert*-butanol. Additionally, protons of the methylene groups adjacent to the sulphur atoms shift to 2.98 ppm from 2.47 ppm upon the formation of the cage and the C–S stretching frequencies of Sb-$\mathbf{1}_{Et}$ show a significant red shift to 672, 622, and 520 cm^{-1} (from 713 and 677 cm^{-1} in $H_3\mathbf{1}_{Et}$). These experimental values were compared with DFT calculated values from monomer Sb-$\mathbf{1}_H$ and dimer $(Sb\text{-}\mathbf{1}_H)_2$ and the frequency values calculated for both are in good agreement with the experimental values from Sb-$\mathbf{1}_{Et}$. To confirm the water stability of the newly prepared compound, a hydrolytic stability test was performed. To a dry DMSO-d_6 solution of Sb-$\mathbf{1}_{Et}$, 10 equivalents of D_2O were added and the chemical shifts of the protons were monitored for 24 hours and no changes were observed (see Fig. S8†).

Regardless of polarity of the solvent used in the synthesis of Sb-$\mathbf{1}_{Et}$, only an amorphous material was recovered as confirmed by powder X-ray diffraction (PXRD) analysis. This was further confirmed by light microscopy where some of the larger particles of Sb-$\mathbf{1}_{Et}$ appeared spherical and translucent, suggesting the formation of hollow spheres. To gain a better understanding of the morphology of Sb-$\mathbf{1}_{Et}$ (as-synthesized), it was subjected to SEM which verified that Sb-$\mathbf{1}_{Et}$ spontaneously forms spherical supramolecular structures (Fig. 2).

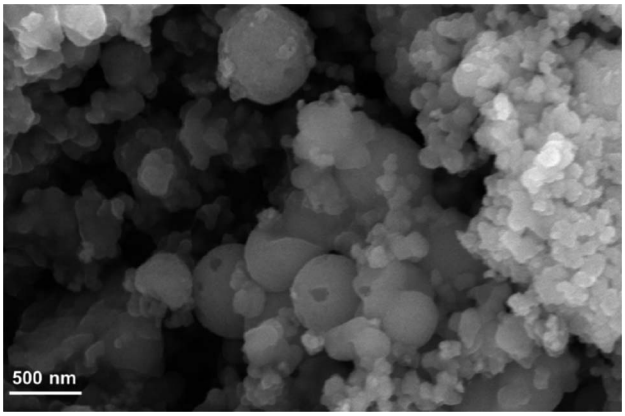

Fig. 2 SEM image of the as-synthesized Sb-$\mathbf{1}_{Et}$.

In situ encapsulation of guest molecules

To investigate whether these spherical structures are hollow or not, a known amount of ferrocene (Fc) was used as a marker molecule to be encapsulated during the synthesis of Sb-$\mathbf{1}_{Et}$ (for more details see S4.1 in ESI†). After removal of the free Fc molecules, the vesicles were lysed and dissolved with DMSO-d_6 and studied by ^{1}H NMR. Characterization of the ruptured vesicles of Sb-$\mathbf{1}_{Et}$ by ^{1}H NMR revealed the presence of the Fc marker molecule and *tert*-butanol (the co-product of the reaction) along with hexanes (the reaction solvent). The theoretical ratio of the protons of Fc compared to protons of *tert*-butanol in the reaction is 0.56. Integrated values from the ^{1}H NMR in Fig. 3 reveal an experimental ratio of 0.58 which is very close to the theoretical value and confirms the ability to form hollow vesicles that encapsulate other chemicals during synthesis. In this case a total of approximately 0.2% of the Fc molecules were captured in the vesicles during their *in situ* formation. A sample was stored and dissolved in DMSO-d_6 after 6 months at ambient conditions. All Fc molecules were still encapsulated inside the vesicles (based on the ratio of Fc protons to methylene cage protons of Sb-$\mathbf{1}_{Et}$). However, the ratio of the Fc protons to *tert*-butanol was not equal to the value obtained initially which suggests that more volatile chemicals (*tert*-butanol and hexanes) can escape vesicles over an extended time period. This behaviour contrasts significantly with the isostructural

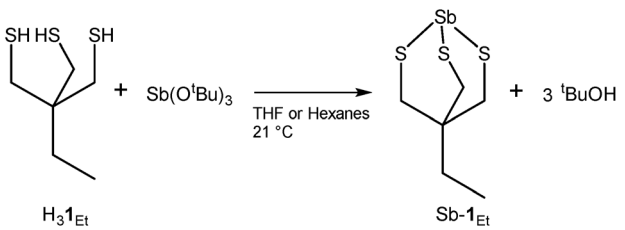

Scheme 1 Preparation of Sb-$\mathbf{1}_{Et}$.

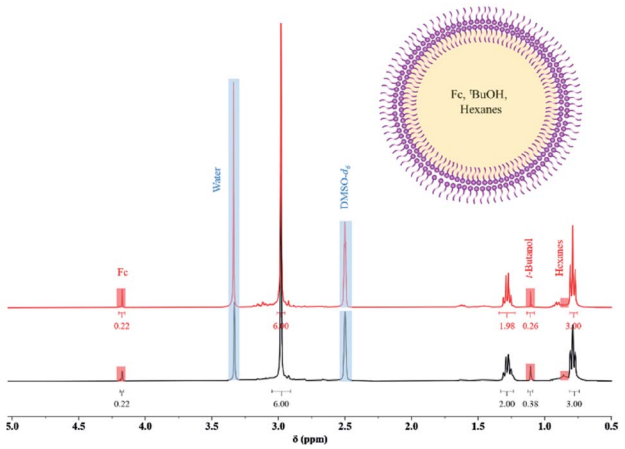

Fig. 3 ^{1}H NMR (black spectrum) of ruptured vesicles in DMSO-d_6 after *in situ* encapsulation and an illustration of a hollow reversed vesicle containing solution it has been synthesized in prior to rupture. ^{1}H NMR (red spectrum) of ruptured vesicles in DMSO-d_6 six months after storing powders in ambient conditions.

Open Access Article. Published on 09 April 2020. Downloaded on 1/22/2026 8:31:17 PM. This article is licensed under a Creative Commons Attribution-NonCommercial 3.0 Unported Licence.

antimony alkoxide cage which is isolated as a crystalline material with a helical columnar supramolecular structure.[25]

Solid-state characterization of antimony thiolate bilayer

X-ray quality single crystals of Sb-$\mathbf{1}_{Et}$ were obtained from the slow evaporation of a solution of Sb-$\mathbf{1}_{Et}$ following sonication in acetonitrile. XRD analysis revealed the anticipated cage structure with three Sb–S primary bonds with average bond distance of 2.444(7) Å as depicted in Fig. 4 which is in agreement with the average reported Sb–S (2.44 Å) bond distance.[33] The longer Sb–S bonds lead to a cage that is significantly more distorted away from C_{3v} symmetry than in alkoxides Sb-$\mathbf{2}_R$ (R = Me, Et, Pr, NHCONon). The Sb–Ch–C angles are significantly more acute in Sb-$\mathbf{1}_{Et}$ (~102°) than in alkoxide Sb-$\mathbf{2}_R$ (~118°).[24,25] In the crystal structure, molecules of Sb-$\mathbf{1}_{Et}$ self-assemble through pnictogen bonds to form a reversed bilayer structure where each antimony interacts with three distinct sulphur atoms (Fig. 4a). Within each layer, every molecule is surrounded by four molecules of Sb-$\mathbf{1}_{Et}$ as shown in Fig. 4b. The Sb atom in the central molecule forms PnBs with two S atoms on adjacent molecules, the $Sb_1\cdots S_{4\text{-}1}$ and $Sb_1\cdots S_{5\text{-}2}$ distances are 3.554(8) Å and 3.707(5) Å respectively, which are 92% and 96% of the $\sum r_{vdW}$ of Sb and S. Two of the sulphur atoms (S_1 and S_2) act as PnB acceptors for the adjacent $Sb_{2\text{-}3}$ and $Sb_{2\text{-}4}$ atoms. The $S_1\cdots Sb_{2\text{-}3}$ and $S_2\cdots Sb_{2\text{-}4}$ bond distances are 3.680(8) Å and 3.500(6) Å, respectively, or 95% and 90% of the $\sum r_{vdW}$ of Sb and S. In addition to the intralayer PnBs depicted in Fig. 4b, each molecule forms a set of interlayer interactions. This set of interactions occurs between molecules in an antiparallel alignment to form a supramolecular synthon that contains two primary Sb–S bonds and two PnBs (Fig. 4c). PnB distances for $Sb_1\cdots S_5$ and $Sb_2\cdots S_1$ in this dimeric unit are shorter than the other PnBs at 3.243(6) Å and 3.260(6) Å which averages to 84% of the $\sum r_{vdW}$. This motif differs slightly from those observed with the antimony alkoxide cages, where every pnictogen bond is with a molecule in the opposing layer.[24,25] The ability of the thiol analogue to form a similar bilayer structure contrasts with $Sb(S_2C_6H_4)SMe$ which does not form a bilayer structure in the solid state whereas the oxygen analogue, $Sb(O_2C_6H_4)OMe$, does.[34] This hints at the importance of the cage structure in promoting a predictable bilayer assembly. The synthesis and crystal structure of the arsenic analogue (As-$\mathbf{1}_{Et}$) has been reported previously. No bilayer structure was observed, rather simple dimers of As-$\mathbf{1}_{Et}$ assembled through two PnBs are observed. The $As_1\cdots S_1$ distance is 3.537 Å which is 97% of the $\sum r_{vdW}$ of As and S.[35] The difference between the number and distances of PnBs formed in As-$\mathbf{1}_{Et}$ and Sb-$\mathbf{1}_{Et}$ illustrates the important role of the heavier elements in the application and design of supramolecular structures. The heavier pnictogen thiolate cages are more Lewis acidic as a result of increasing stereochemical inactivity of the lone pairs and the increasing polarity of the primary bonds. This is in line with findings for the analogous alkoxide cages[36] and is in line with other experimental and computational findings for pnictogen, chalcogen and halogen bonding in the +3, +2 and +1 oxidation states, respectively.[37–42]

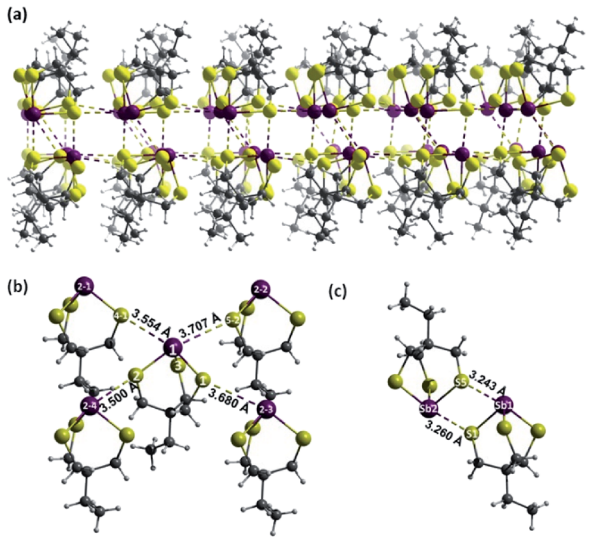

Fig. 4 (a) Reversed bilayer of Sb-$\mathbf{1}_{Et}$ through strong PnBs of Sb and S atoms. (b) Intralayer self-assembly of Sb-$\mathbf{1}_{Et}$. (c) Formation of two strong interlayer PnBs between two Sb-$\mathbf{1}_{Et}$ molecules (Sb: purple, S: yellow, C: grey, H: white).

Computational study of the pnictogen bonding

An often suggested prerequisite for strong PnBs, following studies on halogen and chalcogen bonding, is the presence of large V_{max} (maximum in the electrostatic potential energy surface calculated on a molecular surface at 0.001 au)[43,44] values associated with the electrophilic regions of the ESP surface.[40,45–48] A typical design strategy used to achieve this is to incorporate polar primary bonds. The replacement of O with S to enhance the stability of the primary bonds is therefore expected to result in smaller V_{max} values and weaker PnBs. Given the observed self-assembly, it became of interest to determine the driving force behind the formation of these PnBs as compared with the alkoxide congeners. Molecular geometries and electronic structures were optimized using DFT (B97-D3, ZORA, def2-TZVPP). The electrostatic potential energy (ESP) shown in Fig. 5a and Fukui functions(see Fig. S1 in ESI†) integrated from above ($f^+(r)$) were plotted on the molecular surface (0.001 au) of Sb-$\mathbf{1}_H$ and As-$\mathbf{1}_H$ monomers. Three localized electrophilic regions are observed on the Fukui function. These regions complement the three V_{max} regions on the electrostatic potential surface and serve to give directionality to these interactions. The V_{max} values, however, are intermediate to the analogous antimony alkoxide cage, which forms three pnictogen bonds, and the arsenic alkoxide cage, which only forms one in the solid state suggesting a diminished electrostatic contribution to the Sb···S pnictogen bonds.[36] Despite the lower V_{max} values calculated for Sb-$\mathbf{1}_H$, they are still considerably larger than those calculated for As-$\mathbf{1}_H$ (Fig. 5a) which further supports the use of the heavier pnictogens for stronger and more PnBs.

To gain a better understanding of the ability of Sb-$\mathbf{1}_{Et}$ to form the multiple pnictogen bonds required for reversed bilayer assembly, the energetics of pnictogen bond formation were

 This journal is © The Royal Society of Chemistry 2020

Open Access Article. Published on 09 April 2020. Downloaded on 1/22/2026 8:31:17 PM.
This article is licensed under a Creative Commons Attribution-NonCommercial 3.0 Unported Licence.

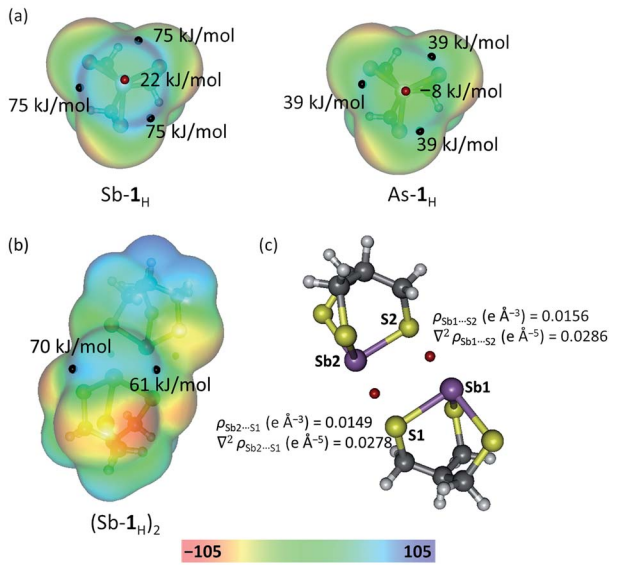

Fig. 5 (a) Electrostatic potential of Sb-$\mathbf{1}_{H}$ and As-$\mathbf{1}_{H}$ monomers, and (b) Sb-$\mathbf{1}_{H}$ dimer mapped on 0.001 au isosurface. Black and red spheres are the positions of V_{max} and V_{min} respectively. (c) Position (red spheres) of PnB BCPs along with values of the electron density and the Laplacian of the electron density in the Sb-$\mathbf{1}_{H}$ dimer.

probed and contrasted with those of the Sb-$\mathbf{2}_{Pr}$ using simplified model systems (see Fig. S2 and Table S2†). The alkoxide dimer (Sb-$\mathbf{2}_{H}$)$_2$, and thiolate dimer (Sb-$\mathbf{1}_{H}$)$_2$ are assembled through two PnBs (as depicted in Fig. S2†) and have dimerization energies of -53 kJ mol^{-1} (average of two crystallographically independent dimers) and -41 kJ mol^{-1}, respectively. To verify the presence of PnBs in the dimer, and probe the role of orbital overlap in stabilizing these interactions, an atoms in molecules (AIM) analysis was performed on (Sb-$\mathbf{1}_{H}$)$_2$ (represented in Fig. 5b). The analysis revealed two bond critical points (BCP) between each Sb and S pair located on the bond path associated with the PnBs in the dimer (Fig. 5c). The densities at the PnB BCPs are 0.0156 and 0.0149 e Å^{-3} for $Sb_1\cdots S_2$ and $Sb_2\cdots S_1$, respectively. These values are consistent with those reported for pnictogen, chalcogen and halogen bonding.[36,39,49] It is noteworthy that the BCP values for (Sb-$\mathbf{1}_{H}$)$_2$ are about 60% smaller than the BCP values for (Sb-$\mathbf{2}_{H}$)$_2$ reported previously.[36] This suggests that, in addition to a diminished electrostatic contribution to the Sb···S PnBs, the covalency is also lower. The near zero, but positive Laplacian of the electron density at the PnB BCPs indicates the closed-shell nature of these interactions.[49] The lower energy associated with (Sb-$\mathbf{1}_{H}$)$_2$ is consistent with the lower electrostatic potentials. This appears to contrast with the ability of these systems to self-assemble into bilayers and spontaneously form spherical structures upon synthesis. It seemed possible that the loss of stabilization from directional electrostatic attraction could be offset by an increase in non-direction London dispersion forces resulting from the increase in polarizability of the chalcogen. Inclusion of dispersion corrections in the energy calculations[50] revealed how important this contribution becomes in the thiolate system. The dispersion-corrected dimerization energy of thiolate (Sb-$\mathbf{1}_{H}$)$_2$ is -97 kJ mol^{-1} which is slightly more than the alkoxide (Sb-$\mathbf{2}_{H}$)$_2$ (-93 kJ mol^{-1}). Dispersion represents 58% of the dimerization energy in (Sb-$\mathbf{1}_{H}$)$_2$ (compared to 43% in (Sb-$\mathbf{2}_{H}$)$_2$). This illustrates the significant role the non-directional London dispersion forces play in reinforcing the directional electrostatic and polarization contributions associated with pnictogen bonding. The role of solvent in stabilizing these bilayers with respect to the monomeric units was not addressed in this study, but it can be expected that solvent plays an important role in this.

Preparation and characterization of vesicles

The as-synthesized vesicles of Sb-$\mathbf{1}_{Et}$ appear to have a very large size distribution (Fig. 2). To control the size distribution of the vesicles, samples were sonicated using a 20 kHz, VCX 750 (Sonics and Materials) ultrasonic probe. Following sonication, particle sizes were measured using a Nanotrac Model NPA250 DLS (Dynamic Light scattering) instrument. Four different parameters, solvent, probe power amplitude, sonication time, and concentration (0.05, 0.10, 0.25, 0.50 mM), were evaluated in order to understand the impact of each. A summary of the findings are provided in Fig. 6 (see S3 in ESI† for full details on all experiments).

The distributions are relatively invariant with respect to all of the parameters except for the nature of the solvent. This contrasts with samples of Sb-$\mathbf{2}_{NHCONon}$, where concentration also has a significant effect on the size distribution of the particles. The size distributions of particles of Sb-$\mathbf{1}_{Et}$ under most conditions tends to centre at 320 nm. These particles are larger than the vesicles observed for Sb-$\mathbf{2}_{NHCONon}$ (~70 nm). Hexanes gave rise to a broader distribution of larger particles. As a result, 5 minutes sonication time and 40% power amplitude were chosen as a standard set of conditions for the preparation of reversed vesicles for further study.

Fig. 7 shows a TEM and SEM image of the vesicles prepared at a concentration of 0.25 mM in wet acetone with a sonication time of 5 minutes and 40% power amplitude. Due to the presence of antimony atoms there is no need to stain the samples for TEM imaging. Both TEM and SEM images support the average size distribution obtained from the DLS measurements.

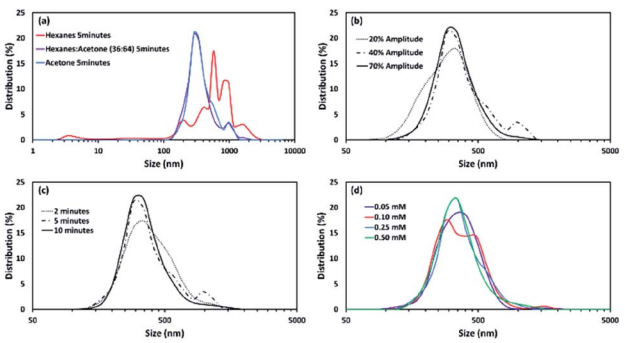

Fig. 6 Effect of (a) solvent at 40% probe power amplitude (0.25 mM), (b) probe power amplitude in acetone (0.25 mM), (c) sonication time in acetone (0.25 mM) with 40% probe power amplitude, and (d) solution concentration (in acetone with 40% probe power amplitude) on the size of vesicles of Sb-$\mathbf{1}_{Et}$.

Open Access Article. Published on 09 April 2020. Downloaded on 1/22/2026 8:31:17 PM.
This article is licensed under a Creative Commons Attribution-NonCommercial 3.0 Unported Licence.

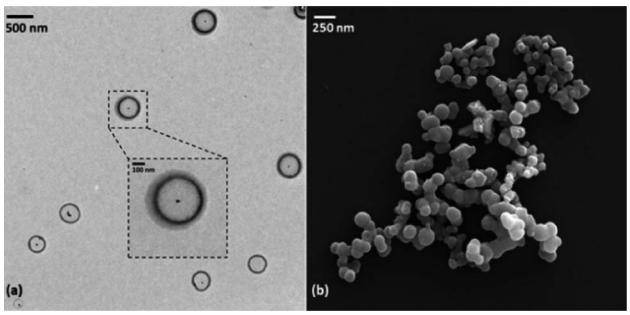

Fig. 7 (a) TEM and (b) SEM images of the prepared vesicles from 0.25 mM acetone solution of Sb-$\mathbf{1}_{Et}$ vesicles were prepared by sonicating the solution mixture for 5 minutes at 40% probe power amplitude.

The SEM images reveal a spherical morphology for these supramolecular structures and the TEM images confirm that these structures are hollow. Taken together with the structural data, a model emerges of hollow vesicles with reversed bilayer membranes held together by pnictogen bonds. Remarkably, images of the same solutions obtained after 90 days show a similar distribution of these structures, indicating a good temporal stability of these vesicles and an excellent tolerance to typical laboratory atmospheric conditions.

To facilitate encapsulation studies in chloroform, vesicle preparation using ultrasound in this solvent was also evaluated. The size distribution of the vesicles prepared in a chloroform solution was not as uniformly distributed as those in acetone (Fig. 8a); a size distribution between 30–1000 nm with three major peaks at 86, 204, and 818 nm was observed. Extrusion has been used with biological membranes to produce uniform vesicle sizes. This strategy was adapted for these vesicles by using an extrusion setup (Avanti Polar Lipids, Inc.) with a hydrophobic PTFE membrane (Cole-Parmer, 0.22 μm pore size) sandwiched between two Teflon holders with o-rings. This membrane was chosen as it is stable to chloroform and other organic solvents, but it should be noted that the pores in these membranes are quite different than the typical track-etched polycarbonante membranes used for vesicles prepared from membranes in aqueous solutions. A 0.25 mM chloroform solution of the vesicles was prepared using an ultrasonic probe (40% power amplitude for five minutes). For each extrusion cycle, a 10 mL sample was extruded portion wise (1 mL at a time) through the membrane. All aliquots were collected in a vial and their size distribution was measured before the next cycle of the extrusion. Five rounds of extrusion yielded vesicles with a uniform and narrow size distribution around 240 nm which is the approximate size of the pores in the membrane(Fig. 8b). To confirm vesicles were still hollow TEM images (Fig. 8c) were collected and demonstrated that the majority are still hollow. However, it appeared that some of the larger vesicles have encapsulated smaller ones during the extrusion process.

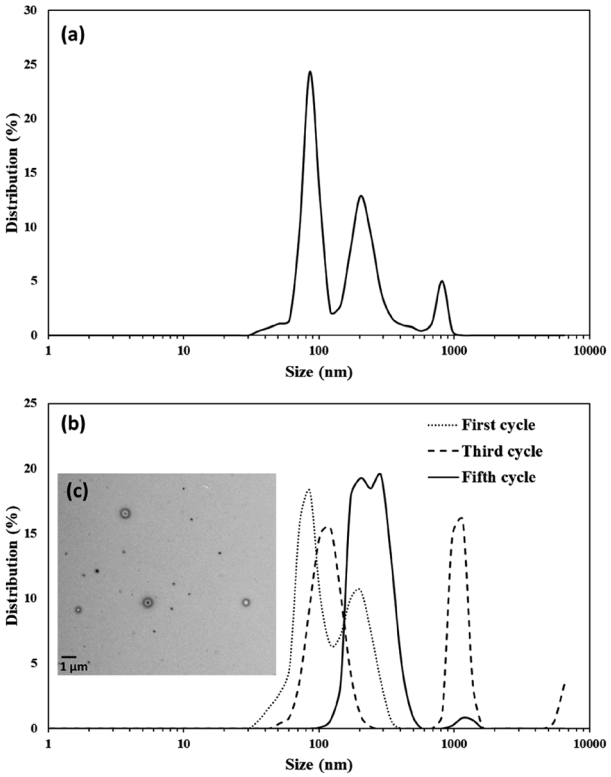

Fig. 8 Size distribution of (a) 0.25 mM chloroform solution of vesicles prepared (b) same vesicle solution extruded for five cycles. (c) TEM image of the extruded vesicles after fifth cycle.

Encapsulation of guest molecules

The ability to make hollow, spherical, and chemically and temporally stable vesicles that can be broken and reformed by sonication indicated that these systems could be useful for encapsulation and compartmentalisation in organic media. To test this, fluorescent dyes rhodamine B (RhB) and an acridone-based (Ac) dye were post-synthetic encapsulated and imaged.[51] To capture the fluorescent dyes, 0.7 mg of RhB, or 0.1 mg of Ac were added to acetone or chloroform, respectively, containing 0.25 mM of Sb-$\mathbf{1}_{Et}$. Both samples were sonicated for 5 minutes at 40% probe power amplitude. Following sonication, each mixture was transferred into a dialysis bag (Spectra/Pro, 6–8 kD) and was dialyzed for 48 hours in the respective solvent, replacing with fresh solvent three times. After dialysis, a drop of the solution was cast on a microscope slide and studied using fluorescence microscopy (for more details see S1.8 in ESI†). The same samples were used for obtaining TEM images (Fig. 9). Fluorescent microscopy images of vesicles with encapsulated Ac are shown in Fig. 9a (for RhB sample see Fig. S34†). The vesicles appear to be more worm-shaped rather than being spherical. TEM (Fig. 9b) revealed that the vesicles retain their spherical shape but have started to aggregate which gives the illusion of elongated shapes in the fluorescence microscope images.

All of the dye encapsulation and dialysis experiments clearly show that the fluorescent dyes have been encapsulated into the vesicles. They can be dialysed and emit only from within the vesicles at their corresponding wavelengths. Solutions of dialyzed samples were stored and re-examined with fluorescence microscopy after 3 months and similar images were obtained indicating that the fluorescent dyes remain within the vesicles (see Fig. S35 and S38†). This suggests that the membrane both

 This journal is © The Royal Society of Chemistry 2020

Open Access Article. Published on 09 April 2020. Downloaded on 1/22/2026 8:31:17 PM.
This article is licensed under a Creative Commons Attribution-NonCommercial 3.0 Unported Licence.

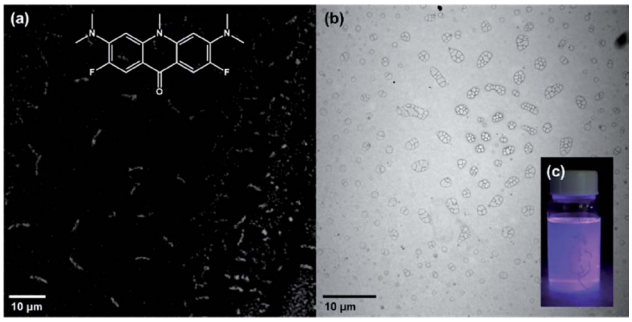

Fig. 9 (a) Fluorescence microscopy images (with enhanced contrast) of the encapsulated Ac (including chemical structure) after dialysis. (b) TEM image of the vesicles after encapsulation and dialysis of Ac (image was taken 14 days after fluorescence imaging). (c) Camera image of vesicles solution after dialysis of excess Ac under 378 nm irradiation.

remains intact and is resistant to passive diffusion of these molecules. An additional experiment was performed with 6-carboxyfluorescein (6-FAM) dye in an acetone solution (for more details see S4.2.2 in ESI†). After dialysis, vesicles were examined *via* optical and fluorescent microscopy (Fig. S36†). Larger vesicles appeared translucent and emitting under blue light which confirmed successful encapsulation of 6-FAM. After collecting the images, a drop of water was cast on the vesicles in order to lyse them and changes in emission were monitored for 20 minutes. After 20 minutes it was noticeable that the number of emitting vesicles were decreasing, and the bulk solution was becoming weakly emissive. A light image was acquired after 20 minute mark and it was observed that many of the vesicles have lysed during exposure to water and started to deflate compared to the initial white light microscopy image that was captured (Fig. S37†).

Encapsulation of ferrocene provides the opportunity to probe the effect of encapsulation by these vesicles on the redox properties of ferrocene. CV (cyclic voltammetry) analysis was performed on a 0.1 M $TBAPF_6$ (tetrabutylammonium hexafluorophosphate) chloroform solution containing Fc (1.6 mM) and Sb-$\mathbf{1}_{Et}$ (0.25 mM) that were sonicated (40% power amplitude) for five minutes. After sonication, the unencapsulated Fc molecules were removed from the bulk solution *via* dialysis. Light microscope images were obtained at this point to confirm the presence of vesicles (Fig. S30†). After dialysis, 2 mL of this solution was diluted with 8 mL of the electrolyte solution. CV measurements were performed in triplicate and the potentials are reported relative to the Fc/Fc^+ redox couple obtained from a 0.15 mM solution of Fc in 0.1 M $TBAPF_6$ in chloroform. The half-wave potential ($E_{1/2}$) for encapsulated Fc was -45 ± 2 mV *vs.* free Fc/Fc^+ which suggests that encapsulation in vesicles of Sb-$\mathbf{1}_{Et}$ facilitates the oxidation of the Fc molecules. A possible model for this behaviour is that electron rich and polarizable membrane in these pnictogen-bonded vesicles stabilizes the charged species better than the bulk solution. To ensure that the observed shift was the result of encapsulation, a mixture of a solution of Fc-containing vesicles and free Fc (0.15 mM) was prepared. The resulting half-wave potential was intermediate to free Fc and encapsulated ferrocene, indicating that both are electrochemically active and are oxidized at different potentials.

Conclusions

A new air and moisture stable bicyclic, trivalent antimony thiolate compound has been designed to engage in triple pnictogen bonding. Structural characterization revealed a self-assembled reversed bilayer. DFT calculations reveal that the directionality of the PnBs arises from electrostatic attraction, but this is reinforced by a large contribution from London dispersion forces. The self-assembly propagates in solution as well, giving rise to the spontaneous formation of hollow reversed vesicles that were demonstrated to alter the half-wave potential of encapsulated ferrocene molecules. The size distribution of these vesicles can be controlled through sonication. In chloroform, extrusion was demonstrated as an efficient method for increasing the uniformity of vesicles. The vesicles have proven to be robust enough to be used as nanocontainers for encapsulation and storage of chemicals in solid and solution states for long periods of time.

Conflicts of interest

There are no conflicts to declare.

Acknowledgements

AFC and SM are grateful for research funding (CHE 1847878) and instrument support (NMR, CHE 1048553 and SEM, MRI 0421032) from the National Science Foundation. SM is indebted to Spring 2019 students of CHEM-3201 and Dr Douglas Pool for the synthesis of Ac. DP would like to acknowledge support from the National Institutes of Health (GM 120669) and National Science Foundation (1849063). We would also like to show our gratitude to the Hope-Weeks and Wylie Labs in the TTU Department of Chemistry and Biochemistry.

Notes and references

1 K. T. Kim, S. A. Meeuwissen, R. J. M. Nolte and J. C. M. van Hest, *Nanoscale*, 2010, **2**, 844–858.
2 *Medical Applications of Liposomes*, 1st edn, https://www.elsevier.com/books/medical-applications-of-liposomes/lasic/978-0-444-82917-7, accessed January 9, 2020.
3 C. Hofmann, A. Duerkop and A. J. Baeumner, *Angew. Chem., Int. Ed.*, 2019, **58**, 12840–12860.
4 D. Grigoriev, E. Shchukina and D. G. Shchukin, *Adv. Mater. Interfaces*, 2017, **4**, 1600318.
5 F. Fernandez-Trillo, L. M. Grover, A. Stephenson-Brown, P. Harrison and P. M. Mendes, *Angew. Chem., Int. Ed.*, 2017, **56**, 3142–3160.
6 H. Pick, A. C. Alves and H. Vogel, *Chem. Rev.*, 2018, **118**, 8598–8654.
7 E. Rideau, R. Dimova, P. Schwille, F. R. Wurm and K. Landfester, *Chem. Soc. Rev.*, 2018, **47**, 8572–8610.

Open Access Article. Published on 09 April 2020. Downloaded on 1/22/2026 8:31:17 PM. This article is licensed under a Creative Commons Attribution-NonCommercial 3.0 Unported Licence.

8 E. Aznar, M. Oroval, L. Pascual, J. R. Murguía, R. Martínez-Máñez and F. Sancenón, *Chem. Rev.*, 2016, **116**, 561–718.
9 R. P. Brinkhuis, F. P. J. T. Rutjes and J. C. M. van Hest, *Polym. Chem.*, 2011, **2**, 1449–1462.
10 J. Gaitzsch, X. Huang and B. Voit, *Chem. Rev.*, 2016, **116**, 1053–1093.
11 D. E. Discher and A. Eisenberg, *Science*, 2002, **297**, 967–973.
12 T. Owen and A. Butler, *Coord. Chem. Rev.*, 2011, **255**, 678–687.
13 J. Voskuhl and B. Jan Ravoo, *Chem. Soc. Rev.*, 2009, **38**, 495–505.
14 T. Nishimura, S. Hirose, Y. Sasaki and K. Akiyoshi, *J. Am. Chem. Soc.*, 2020, **142**, 154–161.
15 Y. Zhu, P. Yin, F. Xiao, D. Li, E. Bitterlich, Z. Xiao, J. Zhang, J. Hao, T. Liu, Y. Wang and Y. Wei, *J. Am. Chem. Soc.*, 2013, **135**, 17155–17160.
16 F. Tosi, M. C. A. Stuart, S. J. Wezenberg and B. L. Feringa, *Angew. Chem., Int. Ed.*, 2019, **58**, 14935–14939.
17 *Synthetic Surfactant Vesicles*, https://www.crcpress.com/Synthetic-Surfactant-Vesicles-Niosomes-and-Other-Non-Phospholipid-Vesicular/Uchegbu/p/book/9789058230119, accessed January 9, 2020.
18 P. Walde, K. Cosentino, H. Engel and P. Stano, *ChemBioChem*, 2010, **11**, 848–865.
19 V. Percec, D. A. Wilson, P. Leowanawat, C. J. Wilson, A. D. Hughes, M. S. Kaucher, D. A. Hammer, D. H. Levine, A. J. Kim, F. S. Bates, K. P. Davis, T. P. Lodge, M. L. Klein, R. H. DeVane, E. Aqad, B. M. Rosen, A. O. Argintaru, M. J. Sienkowska, K. Rissanen, S. Nummelin and J. Ropponen, *Science*, 2010, **328**, 1009–1014.
20 S. E. Sherman, Q. Xiao and V. Percec, *Chem. Rev.*, 2017, **117**, 6538–6631.
21 P. Torre, Q. Xiao, I. Buzzacchera, S. E. Sherman, K. Rahimi, N. Y. Kostina, C. Rodriguez-Emmenegger, M. Möller, C. J. Wilson, M. L. Klein, M. C. Good and V. Percec, *Proc. Natl. Acad. Sci. U. S. A.*, 2019, **116**, 15378–15385.
22 X.-N. Xu, L. Wang and Z.-T. Li, *Chem. Commun.*, 2009, 6634–6636.
23 M. R. Molla and S. Ghosh, *Chem.–Eur. J.*, 2012, **18**, 9860–9869.
24 S. Moaven, J. Yu, M. Vega, D. K. Unruh and A. F. Cozzolino, *Chem. Commun.*, 2018, **54**, 8849–8852.
25 S. Moaven, J. Yu, J. Yasin, D. K. Unruh and A. F. Cozzolino, *Inorg. Chem.*, 2017, **56**, 8372–8380.
26 S. C. Grund, K. Hanusch, H. J. Breunig and H. U. Wolf, *Antimony and Antimony Compounds*, https://onlinelibrary.wiley.com/doi/abs/10.1002/14356007.a03_055.pub2, accessed July 17, 2019.
27 A. Kyono, M. Kimata, M. Matsuhisa, Y. Miyashita and K. Okamoto, *Phys. Chem. Miner.*, 2002, **29**, 254–260.
28 V. M. Cangelosi, M. A. Pitt, W. J. Vickaryous, C. A. Allen, L. N. Zakharov and D. W. Johnson, *Cryst. Growth Des.*, 2010, **10**, 3531–3536.
29 E. Block, G. Ofori-Okai, H. Kang, J. Wu and J. Zubieta, *Inorg. Chem.*, 1991, **30**, 4784–4788.
30 V. M. Cangelosi, L. N. Zakharov and D. W. Johnson, *Angew. Chem., Int. Ed.*, 2010, **49**, 1248–1251.
31 S. A. Fontenot, V. M. Cangelosi, M. A. W. Pitt, A. C. Sather, L. N. Zakharov, O. B. Berryman and D. W. Johnson, *Dalton Trans.*, 2011, **40**, 12125–12131.
32 S. K. Hadjikakou, C. D. Antoniadis, N. Hadjiliadis, M. Kubicki, J. Binolis, S. Karkabounas and K. Charalabopoulos, *Inorg. Chim. Acta*, 2005, **358**, 2861–2866.
33 B. Cordero, V. Gómez, A. E. Platero-Prats, M. Revés, J. Echeverría, E. Cremades, F. Barragán and S. Alvarez, *Dalton Trans.*, 2008, 2832–2838.
34 C. Burschka, *Z. Anorg. Allg. Chem.*, 1978, **446**, 185–192.
35 A. J. DeGraffenreid, Y. Feng, C. L. Barnes, A. R. Ketring, C. S. Cutler and S. S. Jurisson, *Nucl. Med. Biol.*, 2016, **43**, 288–295.
36 H. J. Trubenstein, S. Moaven, M. Vega, D. K. Unruh and A. F. Cozzolino, *New J. Chem.*, 2019, **43**, 14305–14312.
37 A. Bauzá, T. J. Mooibroek and A. Frontera, *ChemPhysChem*, 2016, **17**, 1608–1614.
38 S. Benz, A. I. Poblador-Bahamonde, N. Low-Ders and S. Matile, *Angew. Chem., Int. Ed.*, 2018, **57**, 5408–5412.
39 A. F. Cozzolino, P. J. W. Elder, L. M. Lee and I. Vargas-Baca, *Can. J. Chem.*, 2013, **91**, 338–347.
40 L. Vogel, P. Wonner and S. M. Huber, *Angew. Chem., Int. Ed.*, 2019, **58**, 1880–1891.
41 M. Erdélyi, *Chem. Soc. Rev.*, 2012, **41**, 3547–3557.
42 L. P. Wolters, P. Schyman, M. J. Pavan, W. L. Jorgensen, F. M. Bickelhaupt and S. Kozuch, *Wiley Interdiscip. Rev.: Comput. Mol. Sci.*, 2014, **4**, 523–540.
43 T. Brinck, J. S. Murray and P. Politzer, *Int. J. Quantum Chem.*, 1992, **44**, 57–64.
44 T. Clark, M. Hennemann, J. S. Murray and P. Politzer, *J. Mol. Model.*, 2007, **13**, 291–296.
45 L. C. Gilday, S. W. Robinson, T. A. Barendt, M. J. Langton, B. R. Mullaney and P. D. Beer, *Chem. Rev.*, 2015, **115**, 7118–7195.
46 P. Metrangolo, H. Neukirch, T. Pilati and G. Resnati, *Acc. Chem. Res.*, 2005, **38**, 386–395.
47 M. Michalczyk, W. Zierkiewicz, R. Wysokiński and S. Scheiner, *Molecules*, 2019, **24**, 3329.
48 A. Bauzá, S. K. Seth and A. Frontera, *Coord. Chem. Rev.*, 2019, **384**, 107–125.
49 J.-W. Zou, Y.-X. Lu, Q.-S. Yu, H.-X. Zhang and Y.-J. Jiang, *Chin. J. Chem.*, 2006, **24**, 1709–1715.
50 S. Grimme, J. Antony, S. Ehrlich and H. Krieg, *J. Chem. Phys.*, 2010, **132**, 154104.
51 S. Goodrich, M. Patel and Z. R. Woydziak, *J. Chem. Educ.*, 2015, **92**, 1221–1225.

 This journal is © The Royal Society of Chemistry 2020